AGU PUBLICATIONS

Space Weather

RESEARCH ARTICLE
10.1002/2015SW001223

Key Points:
- Lower atmospheric contributions to ionosphere simulated during the 2009 SSW
- DE2 and DE3 tides are primary drivers of longitudinal variability during this period
- Semidiurnal nonmigrating tides play a role in SSW effects on ionosphere

Correspondence to:
S. E. McDonald,
sarah.mcdonald@nrl.navy.mil

Citation:
McDonald, S. E., F. Sassi, and A. J. Mannucci (2015), SAMI3/SD-WACCM-X simulations of ionospheric variability during northern winter 2009, *Space Weather*, *13*, 568–584, doi:10.1002/2015SW001223.

Received 20 MAY 2015
Accepted 3 AUG 2015
Accepted article online 7 AUG 2015
Published online 17 SEP 2015

SAMI3/SD-WACCM-X simulations of ionospheric variability during northern winter 2009

S. E. McDonald[1], F. Sassi[1], and A. J. Mannucci[2]

[1]Space Science Division, Naval Research Laboratory, Washington, District of Columbia, USA, [2]Jet Propulsion Laboratory, California Institute of Technology, Pasadena, California, USA

Abstract We have performed simulations using the Naval Research Laboratory's physics-based model of the ionosphere, Sami3 is A Model of the Ionosphere (SAMI3), to illustrate how neutral wind dynamics is responsible for day-to-day variability of the ionosphere. We have used neutral winds specified from the extended version of the specified dynamics Whole Atmosphere Community Climate Model (SD-WACCM-X), in which meteorology below 92 km is constrained by atmospheric specifications from an operational weather forecast model and reanalysis. To assess the realism of the simulations against observations, we have carried out a case study during January–February 2009, a dynamically disturbed time characterized by a sudden stratospheric warming (SSW) commencing 24 January 2009. Model results are compared with total electron content (TEC) from Jet Propulsion Laboratory global ionospheric maps. We show that SAMI3/SD-WACCM-X captures longitudinal variability in the equatorial ionization anomaly associated with nonmigrating tides, with strongest contributions coming from the diurnal eastward wave number 2 (DE2) and DE3. Both migrating and nonmigrating tides contribute to significant day-to-day variability, with TEC varying up to 16%. Our simulation during the SSW period reveals that at the Jicamarca longitude (285°E) on 27 January 2009 nonmigrating tides contribute to an enhancement of the electron density in the morning followed by a decrease in the afternoon. An enhancement of the semidiurnal eastward wave number 2 (SE2) and SE3 nonmigrating tides, likely associated with the appearance of the SSW, suggests that these tides increase the longitudinal variability of the SSW impact on the ionosphere. The conclusion is that realistic meteorology propagating upward from the lower atmosphere influences the dynamo region and reproduces aspects of the observed variability in the ionosphere.

1. Introduction

Variability of Earth's thermosphere and ionosphere is primarily associated with the Sun. Indeed, when we think about space weather in the upper atmosphere, the first thought that comes to mind is the enormous impact of coronal mass ejection-driven geomagnetic storms. But during geomagnetically quiet times, and especially during the recent extended solar minimum period of solar cycle 23/24, our attention can turn to the considerable influence the lower atmosphere exerts on the thermosphere/ionosphere; this too can be considered space weather.

It has long been suspected that the lower atmosphere has a profound influence on the ionosphere. Day-to-day and longitudinal variability of the ionosphere not associated with geomagnetic activity has been attributed to processes originating in the lower atmosphere including tides, planetary waves, gravity waves, and even infrasound [*Fraser and Thorpe*, 1976; *Fraser*, 1977; *Forbes and Zhang*, 1997; *Hocke and Schlegel*, 1996; *Laštovička*, 2006]. While meteorological sources have been cited as the origin of much of the day-to-day variability in the ionosphere, only recently have we begun to understand the mechanisms connecting the lower atmosphere to the ionosphere. It is now recognized that upward propagating tides, planetary waves, and gravity waves can couple into the ionosphere through modification of thermospheric composition, influences on *E* region conductivities, modulation of thermospheric temperature and wind structure, and generation of electric fields through dynamo action [*Forbes et al.*, 2000].

Immel et al. [2006] linked a four-peaked, or wave 4, longitudinal pattern in atomic oxygen airglow at 135.6 nm in the low-latitude ionosphere to nonmigrating tides of tropospheric origin. They postulated that these tides propagate into the lower thermosphere and affect the *E* region dynamo processes. Model simulations have since confirmed that nonmigrating tidal modulation of the winds in the *E* region ionosphere sufficiently affects the amplitude of the daytime vertical $E \times B$ drift and produces wavelike features visible in the electron densities when observed at constant local time [e.g., *England et al.*, 2006; *Hagan et al.*, 2007; *Jin et al.*, 2008].

Changes in the thermospheric composition, temperature, and *F* region winds also contribute [*England et al*., 2008]. A comprehensive review of the numerous studies inspired by the work of *Immel et al.* [2006] is provided by *England* [2011].

To capture not only longitudinal but day-to-day variability, ionospheric models must include a thermosphere driven by lower atmospheric weather; to this end, various efforts to couple ionospheric models with the lower atmosphere are underway. The Ground-to-Topside Model of Atmosphere and Ionosphere for Aeronomy (GAIA) is a fully coupled atmosphere-ionosphere model [*Jin et al*., 2011], which includes a whole atmospheric global climate model [*Miyoshi and Fujiwara*, 2003] covering the atmospheric region from the ground to the exobase. The 30 day GAIA free-running simulation for an equinox month (September, $F_{10.7} = 135.0$) shows that day-to-day variation of the longitude structure of the ionosphere is highly variable, but the wave 4 pattern in the daytime equatorial ionization anomaly (EIA) shows up as an average feature. Day-to-day variability has also been studied using the Integrated Dynamics through Earth's Atmosphere (IDEA) model, which consists of the Whole Atmosphere Model (WAM) [*Akmaev et al*., 2008; *Fuller-Rowell et al*., 2008, 2011] coupled with the Global Ionosphere Plasmasphere (GIP) model. *Fang et al.* [2013] used GIP with a one-way coupling to WAM winds to study day-to-day variability of the ionosphere under fixed solar and geomagnetic conditions. *Liu et al.* [2013] demonstrated day-to-day variability of the ionosphere during January–February 2006 using the thermosphere-ionosphere-mesosphere electrodynamics general circulation model (TIME-GCM) constrained up to the mesopause by hourly temperature and horizontal winds provided by the extended version of the Whole Atmosphere Community Climate Model (WACCM-X). The WACCM-X simulations were constrained by the meteorology of NASA/Modern-Era Retrospective Analysis for Research and Applications (MERRA). The TIME-GCM simulations were shown to capture ~50% of the observed variability in the $E \times B$ drifts and F_2 region peak electron density (N_mF_2).

When coupled atmosphere-ionosphere models are constrained with lower atmospheric data, they can be used as exploratory tools to understand observations that suggest connections between the troposphere/stratosphere and the ionosphere. An excellent example is the recent observational evidence that sudden stratospheric warming (SSW) events impact the ionosphere [*Chau et al*., 2009; *Goncharenko et al*., 2010a, 2010b]. There are now a number of modeling studies that have investigated the mechanisms coupling SSW events to the upper atmosphere. The strong SSW event of January 2009 has been particularly well studied. *Fuller-Rowell et al.* [2011] used CTIPe (Coupled Thermosphere-Ionosphere-Plasmasphere electrodynamics) model driven with winds from a version of WAM that has been integrated into a data assimilation system [*Wang et al*., 2011] to reproduce the observed ionospheric variations at Jicamarca that are attributed to changes in the semidiurnal (SW2) and terdiurnal (TW3) migrating tides. WAM coupled with CTIPe was also used to study the longitudinal variations in the ionosphere during the SSW [*Fang et al*., 2012]. In a follow-on study, the IDEA model was used to forecast this SSW event [*Wang et al*., 2014] and demonstrated that amplitude and phase change in SW2. *Pedatella et al.* [2014b] used TIME-GCM with winds and temperatures from WACCM-X applied at the lower boundary at 10 hPa (roughly 30 km) to study the 2009 SSW and showed that the SW2 and semidiurnal lunar tide are important drivers of the ionospheric changes due to the SSW. In this case, the WACCM-X simulations were constrained by both NASA/MERRA and the Navy Operational Global Atmospheric Prediction System–Advanced Level Physics High Altitude (NOGAPS-ALPHA), as described in *Sassi et al.* [2013]. The January 2009 SSW event has also been simulated with a version of GAIA that included assimilation of meteorological reanalysis data [*Jin et al*., 2012].

Although modeling and observational studies are beginning to reveal aspects of day-to-day ionospheric variability due to the lower atmosphere, we are only in the early stages of understanding which components of the lower atmosphere contribute to the observed variations. To investigate sources of day-to-day variability, we use an ionospheric model coupled with winds from a whole atmosphere model to study the period between January and February 2009. This is a geomagnetically quiet time, but it is also characterized by the major sudden stratospheric warming event that commenced in the stratosphere on 24 January. We compare our model results with global ionospheric maps of total electron content (TEC).

2. Models and Data

2.1. Specified Dynamics WACCM-X

The Whole Atmosphere Community Climate Model (WACCM) is a build option of the National Center for Atmospheric Research Community Earth System Model version 1 and can be used in place of the standard atmospheric model. In its standard configuration, WACCM has 66 vertical levels from the ground to about 5.9×10^{-6} hPa (~140 km geometric height). See *Garcia et al.* [2007] for a detailed discussion of the model climate and parameterizations. WACCM can be configured into an extended version (WACCM-X) that incorporates all the features present in the regular configuration with the top boundary located in the upper thermosphere (2.5×10^{-9} hPa or ~500 km altitude). A detailed description of WACCM-X is given in *Liu et al.* [2010]. It should be noted that WACCM-X does not include plasma transport, but a simplified ion drag parameterization is present [see *Sassi et al.*, 2002]. With the vertical extension of the model and the additional physics of the thermosphere, the time step for integration of the physics is 300 s.

WACCM-X can be used to simulate specific events by constraining the model meteorology with data analysis products or observations, using specified sea surface temperature at the lower boundary, and reconstructed spectral irradiances for the historical periods. The initial concepts and results from this model configuration, which is known as the specified dynamics WACCM-X (SD-WACCM-X), can be found in *Marsh* [2011]. In this model configuration the winds and temperature are relaxed toward a set of analyses or observations. These atmospheric specifications are a combination of NASA/MERRA up to about 30 km and Navy's NOGAPS-ALPHA up to 92 km. A detailed discussion of the SD-WACCM-X simulations of January and February 2009, which we use in the current study, can be found in *Sassi et al.* [2013] and *Sassi and Liu* [2014].

2.2. Sami3 Is A Model of the Ionosphere

SAMI3 (Sami3 is A Model of the Ionosphere) is a comprehensive, three-dimensional, physics-based model of the ionosphere developed at the Naval Research Laboratory (NRL). SAMI3 is based on SAMI2 [*Huba et al.*, 2000], a two-dimensional model of the ionosphere. SAMI3 models the plasma and chemical evolution of seven ion species (H^+, He^+, N^+, O^+, $N_2{}^+$, NO^+, and $O_2{}^+$) in the altitude range extending from 85 km to ~8 R_E and latitudes up to ±88°. Unique among ionospheric models, SAMI3 solves the ion continuity and momentum equations for all seven of the ion species and solves the complete temperature equations for the electrons and three ion species (H^+, He^+, and O^+). Ion inertia is included in the ion momentum equation for motion along the geomagnetic field. SAMI3 is the only global ionosphere code that models full plasma transport for all of these ion species, including the molecular ions. Currently, the magnetic field in SAMI3 is represented by an offset, tilted dipole. SAMI3 includes a potential solver to self-consistently solve for the electric fields. The potential equation is derived from current conservation ($\nabla \cdot \mathbf{J} = 0$) in magnetic (currently magnetic-dipole) coordinates, using Ohm's law and including gravity-driven currents. The perpendicular electric field is used self-consistently in SAMI3 to calculate the $E \times B$ drifts [*Huba et al.*, 2008, 2010].

Solar extreme ultraviolet (EUV) irradiances are determined from the NRL Solar Spectral Irradiance (NRLSSI) model [*Lean et al.*, 2011]. NRLSSI calculates the Sun's EUV irradiance in 1 nm bins from 0 to 120 nm using parameters derived from multiple regression of the Mg II and $F_{10.7}$ solar activity indices with irradiance observations made by the Solar EUV Experiment on the Thermosphere Ionosphere Mesosphere Energetic and Dynamics (TIMED) spacecraft since 2002 [*Woods et al.*, 2005]. In its standard configuration, SAMI3 uses Naval Research Laboratory Mass Spectrometer Incoherent Scatter (NRLMSIS) [*Picone et al.*, 2003] to specify thermospheric composition and neutral temperature. The zonal and meridional horizontal winds are typically specified from climatology, such as horizontal wind model (HWM) 07 [*Drob et al.*, 2008] or the updated HWM14 [*Drob et al.*, 2015]. To introduce day-to-day variability into SAMI3, we use hourly winds provided by output from the SD-WACCM-X as described above.

2.3. Jet Propulsion Laboratory Global Ionospheric Maps of Total Electron Content

The SAMI3 simulations are compared with global ionosphere maps (GIMs) of the total electron content (TEC) generated at Jet Propulsion Laboratory (JPL). The JPL TEC product uses a global network of ~200 GPS receivers to generate global maps. The line-of-sight TEC measurements are converted to vertical TEC using an ionospheric shell model. The vertical TEC is mapped onto basis functions, based on bicubic splines, to interpolate the TEC onto a global grid to create the global maps. A detailed description of the algorithms is described in *Mannucci et al.* [1998], with updated horizontal basis functions as described in *Mannucci et al.* [1999]. For this study we use maps with a temporal resolution of 15 min and a spatial resolution of 5° in longitude and 2.5° in latitude to adequately resolve the longitudinal variations in TEC.

2.4. Simulations

We are interested in quantifying the variability in the ionosphere introduced by the meteorology of the lower atmosphere. It is therefore instructive to run SAMI3 with several different wind fields. Before discussing the differences in the simulations, we first specify the configuration that is consistent among the runs. Each set of runs is performed for the month of January 2009, where we use the daily *Ap* and $F_{10.7}$ for each day. During this exceedingly quiet month, the median *Ap* is 4, with a maximum of 11; the median $F_{10.7}$ is 67 solar flux unit (sfu) and ranges from 66 to 69 sfu. Because NRLMSIS does not reproduce the anomalously low thermospheric density of the recent solar minimum, scalar parameters are applied to the composition and temperature profiles to match global mass density measurements derived from orbital data [*Emmert et al.*, 2008]. We use a scalar of 0.96 for the temperature, 0.77 for oxygen, and 0.93 for all other constituents.

We perform three sets of simulations with different winds. The first set uses HWM14 and serves as the climatological run. The second set of simulations is performed using SD-WACCM-X, which includes both migrating and nonmigrating tides. In the third set of runs, we filter out the most significant nonmigrating tides from the SD-WACCM-X wind profiles; removed tides include DE1, SE1, SW1, DE2, SE2, DW2, and TE3. SAMI3 uses the profile of the SD-WACCM-X winds (both unfiltered and filtered) from 85 km up to ~500 km (2.5×10^{-6} hPa), with velocities assumed constant above this altitude.

3. Results

3.1. The Ionosphere in January 2009

The most important process controlling the large-scale distribution of plasma in the low-latitude region is the zonal (east-west) dynamo electric field that drives a vertical $E \times B$ drift of *F* region plasma at the equator. During the daytime, due to the high conductivity in the *E* region ionosphere, the global *E* region winds and tides control the electric field that leads to an uplift of plasma at the magnetic equator. Subsequent diffusion down the field lines, aided by gravity, results in bands of enhanced plasma density on either side of the magnetic equator, which are collectively known as the equatorial ionization anomaly (EIA) [*Namba and Maeda*, 1939; *Appleton*, 1946] and shows prominently in the global TEC. Models of tides that reach *E* region altitudes have been shown to significantly modulate the zonal electric fields and thus the $E \times B$ drift and EIA [*Hagan et al.*, 2007; *England et al.*, 2008]. Thus, by looking at the TEC and $E \times B$ drifts of our simulations, we illustrate the electrodynamic processes by which the neutral winds affect the ionosphere.

Before considering day-to-day variations of the ionosphere, we first consider the average behavior in January 2009 so that we can examine the extent to which the SAMI3 simulations reproduce major features associated with tides originating in the lower atmosphere. In Figure 1a, we show the JPL TEC at a constant local time (14:00 LT) averaged over the 10 day period, 6–15 January 2009. The mid-to-late afternoon is typically the time period during which the EIA is strongest, due to the integrated effect of the upward vertical plasma drifts over the previous several hours. The longitudinal structure varies from day to day, but averaging over multiple days reveals a wave 3 pattern in the longitudinal structure of the EIA. This wave 3 feature has been observed during northern winter in previous studies [e.g., *Scherliess et al.*, 2008; *Kil et al.*, 2008] and is primarily attributed to the DE2 nonmigrating tide.

Figures 1b–1d show the SAMI3 TEC at 14:00 LT averaged over 6–15 January 2009 for the simulations with SD-WACCM-X winds (Figure 1b), SD-WACCM-X filtered winds (Figure 1c), and HWM14 (Figure 1d). The TEC integration in SAMI3 is performed from 85 km to 20,000 km. In comparison with the JPL TEC (Figure 1a), the simulation with SD-WACCM-X winds (Figure 1b) reproduces the wave 3 feature in the EIA, albeit with some shifts in the strength and location of the crests. When the nonmigrating tides are removed from the winds (Figure 1c), the wave 3 pattern disappears; the remaining longitudinal variation is associated with the offset of the geographic and magnetic equators [*McDonald et al.*, 2008]. We can directly compare this result to the SAMI3 simulations using HWM14 winds (Figure 1d), since HWM14 does not include a parameterization for nonmigrating tides. To first order, the filtered SD-WACCM-X winds produce similar results to HWM14 and offer assurance that the SD-WACCM-X wind climatology is reasonable. We note, however, some differences in the longitudinal variation produced by the SD-WACCM-X-filtered winds versus HWM14. The HWM14 winds also better reproduce the asymmetry in the northern and southern EIA crests, as seen in the JPL TEC.

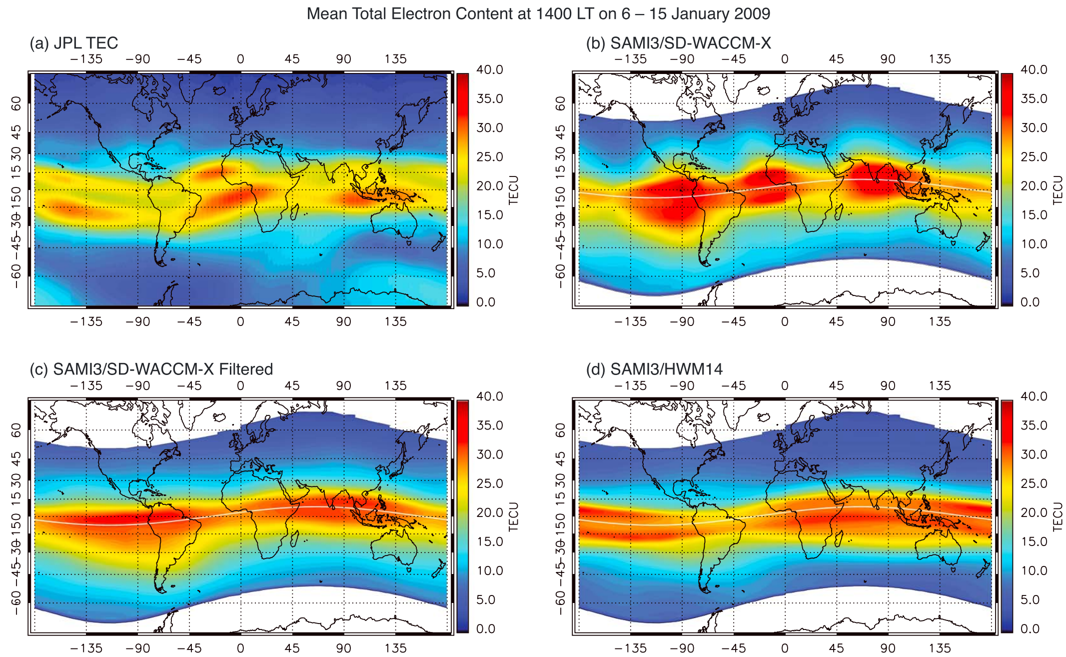

Figure 1. Mean TEC at 14:00 LT on 6–15 January 2009 for (a) JPL TEC maps, (b) SAMI3 with WACCM-X winds, (c) SAMI3 with filtered WACCM-X winds, and (d) SAMI3 with HWM14.

Figure 2b presents the SAMI3/SD-WACCM-X mean vertical plasma drift for 6–15 January 2009 at 300 km altitude. The SAMI3/SD-WACCM-X daytime drifts exhibit a wave 3 longitudinal structure peaking at about 11:00 LT. This structure is consistent with the vertical drift climatology for northern winter based on ROCSAT-1 observations [*Fejer et al.*, 2008; *Kil et al.*, 2008]. Figure 2c shows the drifts for the filtered wind simulation. Without the nonmigrating tides, the wave 3 structure disappears and the peak daytime drift shifts to 12:00 LT. A comparison of Figure 2c to Figure 2b shows that the longitudinal variations generated by nonmigrating tides extend to all local times, including the early evening hours in which a prereversal enhancement of the drifts, largely associated with the *F* region wind dynamo [*Millward et al.*, 2001], is often observed. The pronounced longitudinal variations in the nighttime drift patterns suggest that the *F* region WACCM winds are strongly modulated by the nonmigrating tides. The reduced longitudinal variation in the drifts associated with the filtered winds is similar to the drifts produced with HWM14 (Figure 2d); this is expected since HWM14 does not include nonmigrating tides. Both Figures 2c and 2d can be compared with the Scherliess-Fejer (SF) climatological vertical drift model [*Scherliess and Fejer*, 1999] shown in Figure 2a, which also does not resolve nonmigrating tides. We note that SAMI3 produces weaker drifts compared to the SF model.

Overall, the summary figures of TEC and vertical drifts show that SAMI3, when driven with SD-WACCM-X winds, captures the longitudinal variations associated with nonmigrating tides.

3.2. Ionospheric Day-to-Day Variability

Having established the average behavior of the ionosphere in January prior to the SSW, we now address the day-to-day variability at the time of the large stratospheric warming event of 24 January 2009. The goal is to describe the changes of day-to-day variability induced by the meteorological winds during a dynamically disturbed time and compare to simulations that use the climatological (HWM14) and filtered winds. Such comparisons evince the strong and statistically relevant influence of meteorological winds in general.

Figure 3 illustrates the day-to-day variability of TEC and $E \times B$ vertical drifts at the magnetic equator for the three sets of SAMI3 simulations during 6–31 January 2009. TEC at the Jicamarca longitude (285°E), in the northern EIA crest at 0°N, is shown in Figures 3a–3c. In Figures 3d–3f, the vertical plasma drifts are shown at the magnetic equator and 300 km altitude. The black line represents the average behavior for this period, and the red line indicates the TEC and drift pattern for 27 January 2009, a few days after the SSW event. Individual days are shown in gray, and the yellow shaded area denotes the 1 sigma standard deviation. Considerable day-to-day variability is exhibited by the TEC and vertical drifts in the SAMI3/SD-WACCM-X simulation that includes both

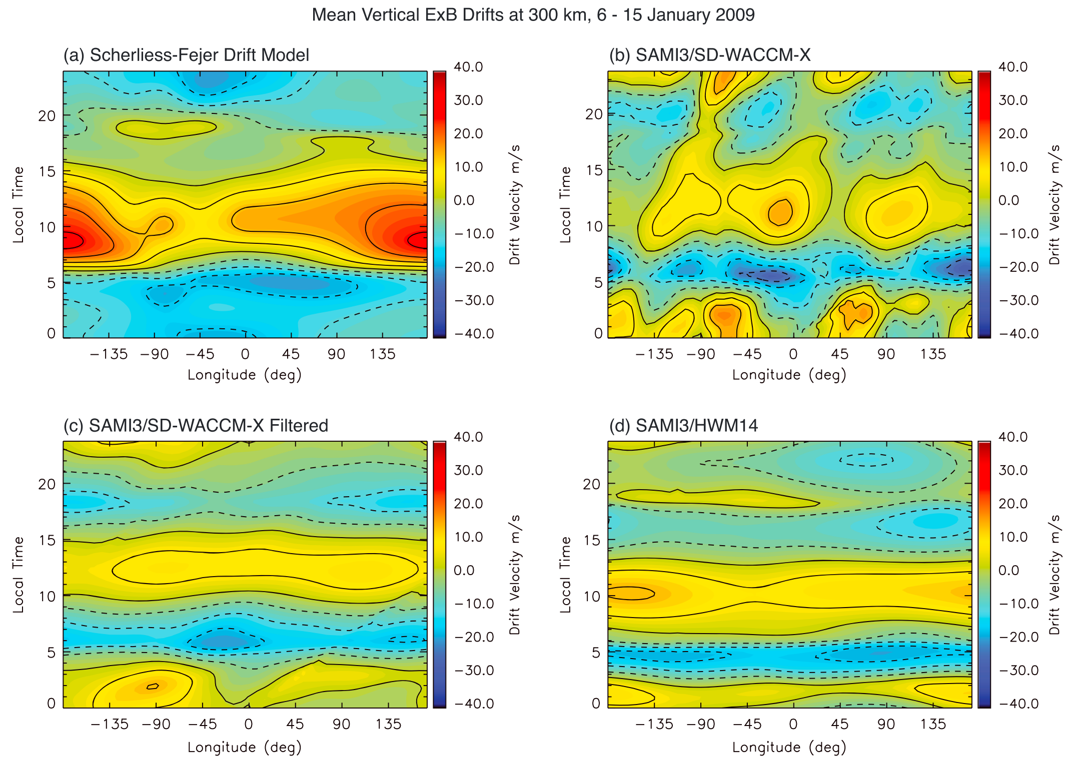

Figure 2. Mean vertical $E \times B$ drifts as a function of geographic longitude and local time at the magnetic equator and 300 km altitude on 6–15 January 2009 for (a) the empirical Scherliess-Fejer drift model, (b) SAMI3 with WACCM-X winds, (c) SAMI3 with filtered WACCM-X winds, and (d) SAMI3 with HWM14.

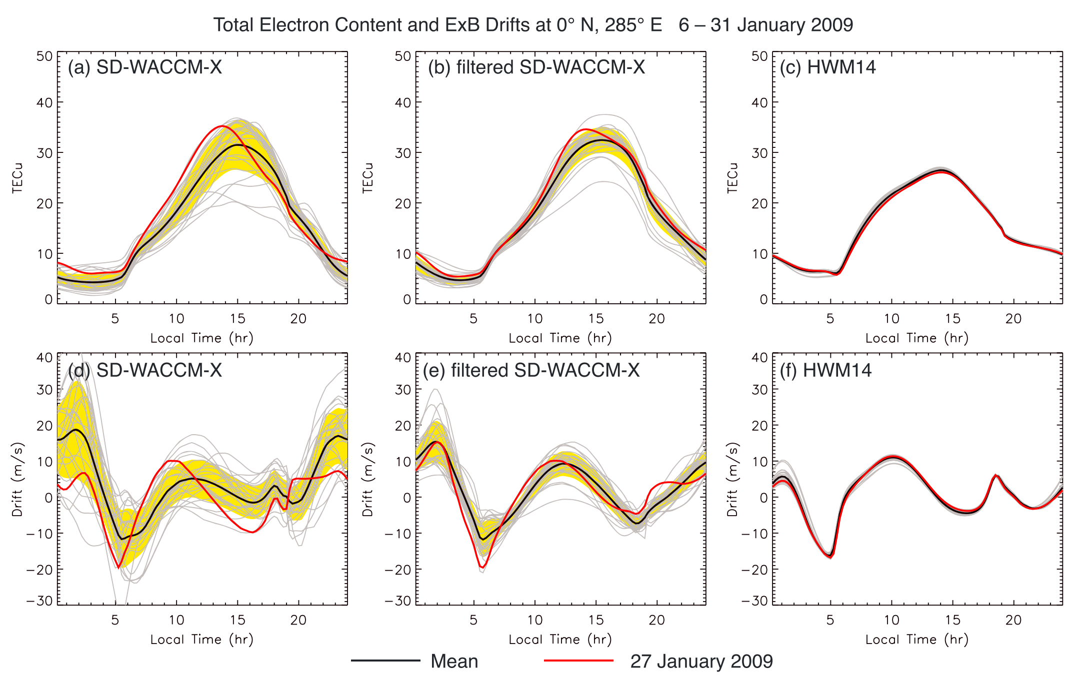

Figure 3. TEC at the Jicamarca longitude (285°E, 0°N) as a function of local time for (a) SAMI3 with WACCM-X winds, (b) SAMI3 with filtered WACCM-X winds, and (c) SAMI3 with HWM14. (d–f) Vertical $E \times B$ drifts at the same location for the same simulations as in Figures 3a–3c. The gray lines show the TEC and vertical drift for each day between 6 and 31 January 2009. The thick black line is the mean over this period, and the thick red line indicates the value on 27 January 2009 after the SSW event.

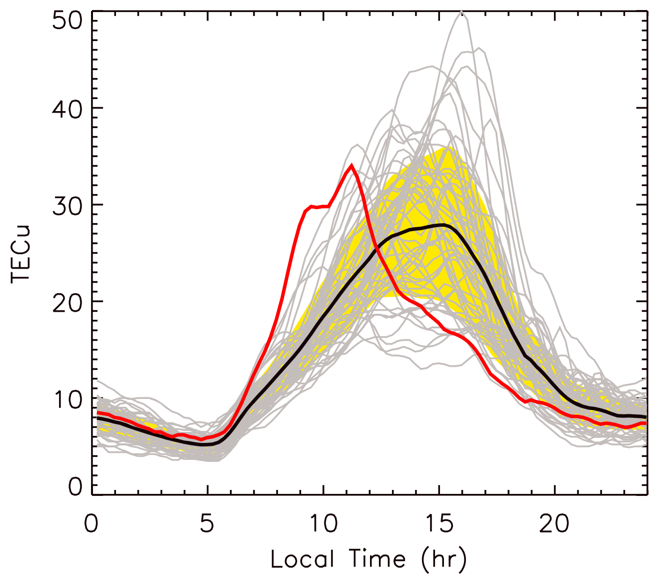

Figure 4. JPL TEC at the Jicamarca longitude (285°E, 0°N) as a function of local time for days between 6 and 31 January 2009. The gray lines show the TEC on each day, the thick black line is the mean TEC over this period, and the thick red lines indicate the TEC on 27 January 2009.

migrating and nonmigrating tides (Figures 3a and 3d). The largest variation in TEC occurs at 15:00 LT, when the density peaks, with a standard deviation of ±5 total electron content unit, 1 TECU = 10^{16} el m^{-2} (which corresponds to a variation of ±16% about the mean). The variation in the vertical drift is more uniform throughout the daytime hours and has a 1 sigma standard deviation of 5 m s^{-1}. The variability decreases by about one half when the nonmigrating tides are removed (Figures 3b and 3e) and nearly disappears altogether in the SAMI3/HWM14 climatological simulations (Figures 3c and 3f). We note that the SAMI3/SD-WACCM-X simulations exhibit significant variability in the nighttime drifts and will be addressed in more detail in the Discussion section.

Goncharenko et al. [2010b] reported observations of the ionospheric response to the large stratospheric warming on 24 January 2009. The vertical drift recorded by the Jicamarca incoherent scatter radar (12°S, 285°E) indicated larger than average upward drifts in the morning hours and downward drifts in the early afternoon hours on 27 January 2009, a few days after the peak in the SSW in the stratosphere. In Figure 3a the red curve shows a similar pattern to the Jicamarca observations. The daytime drift peaks at 10:00 LT and turns negative after 12:00 LT. The simulated result lacks the amplitude of the observed drift (cf. Figure 1e in *Goncharenko et al.* [2010b]), but the phase of the perturbation matches the observations quite well. When the nonmigrating tides are removed (Figure 3b) the feature nearly disappears; thus, in our simulations, the nonmigrating tides are the main driver of the perturbation on 27 January at the Jicamarca longitude.

For reference, we show the JPL TEC (0°N, 285°E) in Figure 4 for the January days. As with the SAMI3 simulations, the maximum TEC occurs at 15:00 LT. The 1 sigma standard deviation is ±5 TECU, which corresponds to 30% variability, nearly twice that of the SAMI3 simulations. The SSW day shows a marked departure from the average behavior over the month. Daytime TEC sharply increases in the early morning hours, peaking just after 11:00 LT, then rapidly declines in the afternoon as the $E \times B$ drift reverses direction.

Whether or not the 27 January perturbation is directly associated with the SSW event is difficult to determine; the day-to-day variability is quite large, and the response after the SSW (red line) is only modestly larger than the day-to-day variability during this period. In the next section, we analyze the neutral winds to elucidate the tides that most strongly contribute to day-to-day variability as well as the SSW feature on 27 January.

3.3. Neutral Wind Tides

In this section, we will focus our attention on the nonmigrating tides, since we have shown above that in our simulations the ionospheric response to the SSW results from the nonmigrating tidal components of the SD-WACCM-X winds. However, we note that the migrating diurnal (DW1) and semidiurnal tides (SW2) play dominant roles in the *E* and *F* region dynamos and account for a significant fraction of the day-to-day variability in the ionosphere, as illustrated in Figures 3b and 3e. Detailed discussion of the prominent migrating tides (DW1 and SW2), including their amplitudes, phase, and temporal behavior, can be found in *Sassi et al.* [2013]. They find that during the January–February 2009 time frame, the DW1 amplitude at 100 km reaches a minimum between 21 January and 31 January. SW2 at the same altitude minimizes from 21 January to 25 January and peaks in early February in the southern hemisphere. In a different study, comparison of SD-WACCM-X to three other whole atmosphere models (GAIA, Hamburg Model of the Neutral and Ionized Atmosphere, and WAM) [*Pedatella et al.*, 2014a] showed that the amplitude and temporal evolution of DW1 during the SSW is similar among all the models. The evolution of the SW2 is also similar in all four

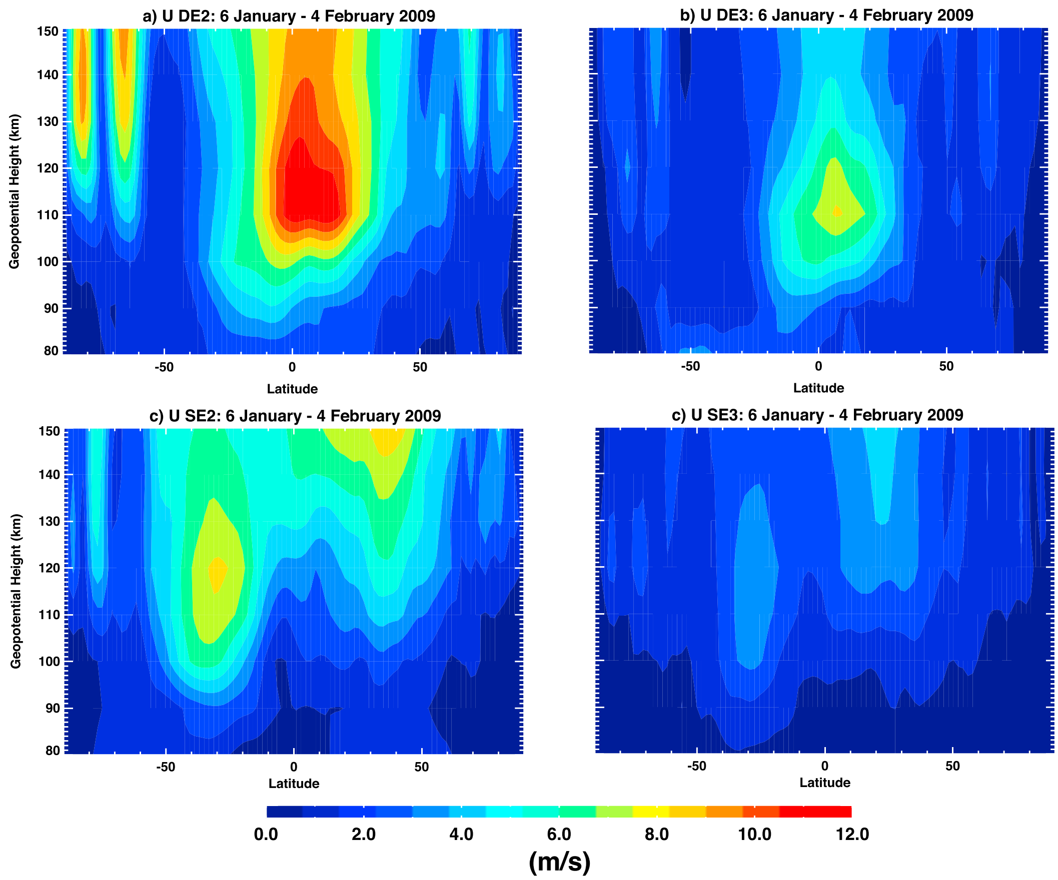

Figure 5. WACCM-X average nonmigrating tides over 6 January to 4 February 2009 for the zonal wind spectrally filtered for (a) DE2, (b) DE3, (c) SE2, and (d) SE3 tides.

models, but there are significant differences in the absolute SW2 amplitudes. Notably, the SW2 amplitude is significantly weaker in SD-WACCM-X than in the other three models; implications of this result are presented in the Discussion section.

We now turn our attention to the significant nonmigrating tides in SD-WACCM-X. In Figure 5, we show the root-mean-square (RMS) amplitude—averaged between 6 January and 4 February 2009—of the zonal wind filtered for the spectral windows corresponding to the nonmigrating tide DE2 (frequency range between 0.8 and 1.2 cpd, for wave number 2; Figure 5a), DE3 (frequencies in 0.8–1.2 cpd, for wave number 3; Figure 5b), SE2 (frequencies in 1.8–2.2 cpd, for wave number 2; Figure 5c), and SE3 (frequencies in 1.8–22 cpd, for wave number 3; Figure 5d). These tides include the nonmigrating modes that contribute to the multicell patterns in the longitudinal variation of the ionosphere [i.e., *Immel et al*., 2006] and can be responsible for the anomalous behavior calculated after the SSW. The vertically propagating DE2 and DE3 tides, along with the SE2 and SE3 tides in this study, are associated with latent heat release from tropospheric convection over low-latitude landmasses. The amplitudes of the diurnal nonmigrating tides (DE2 and DE3) peak at the equator, between 110 and 120 km. The DE2 is generally stronger than DE3, not only in the region where the Hall conductivity peaks (~110–120 km) but also at higher altitudes where the Pedersen conductivity dominates. The large amplitude of the DE2 along with its large-scale height is the reason for the strong wave 3 pattern in the $E \times B$ drifts and electron content. The nonmigrating semidiurnal tides (SE2 and SE3) peak off the equator; the largest amplitudes are found in austral summer between 30°S and 40°S, between 110 and 120 km. Of the two tides, SE2 has much larger amplitude (about 2X) during this time period. Note that in the time averages of Figure 5, the amplitude of the semidiurnal tides is in general smaller than that of the diurnal tides, although the anomalous ionospheric variability detected in observations is of the semidiurnal type. We also note that SE2 extends toward the equator with substantial amplitude above 130 km.

The RMS amplitude illustrates the time mean behavior, but it does not explain the vertical structure of the tides nor does it illustrate the extent of the coherent behavior and its phase. Information about the coherence leads to the meridional and vertical extent of the filtered behavior with an associated measure of statistical significance; the phase, instead, illustrates the vertical depth of the spectral behavior and thus the potential of coupling with the ionosphere dynamo. We use the *Hayashi*'s [1971] formulation to calculate the phase and coherence squared in each spectral window of these nonmigrating tides; in addition, we follow *Julian* [1972] to identify the minimum value of coherence squared that is associated with a statistical significance better than 99%.

Figure 6 again shows the amplitude of the tidal oscillations for the dominant nonmigrating tides. Note that the amplitudes are expected to be slightly smaller than in Figure 5 because of the spectral smoothing applied to increase the degrees of freedom beyond 2 in the periodogram. The white lines depict the ranges of latitudes and altitudes where the behavior is coherent with respect to a reference point at 120 km, denoted by a white *X*, with statistical confidence better than 99%. The reference point is chosen at the equator within the altitude range where the Hall and Pedersen conductivities typically peak during the daytime. To first order, the wave components that efficiently produce dynamo electric fields have broad latitudinal extent and long vertical wavelengths, such that the direction does not shift significantly over the region of high conductivity [*Richmond*, 1995; *Forbes et al*., 2008]. The phase of the spectrally filtered behavior is shown in red and plotted between 45°S and 45°N. While the amplitude spectra are generally consistent with the time-averaged RMS, the regions enclosed by the white lines identify a coherent behavior throughout the regions where the conductivities peak. Moreover, the vertical wavelengths illustrate clearly that these nonmigrating tides are vertically deep (at least 40 km) and can plausibly contribute to the dynamo electric fields that drive the equatorial $E \times B$ drifts.

Next, we delve further into the analysis of temporal variability in order to understand the association of ionospheric TEC changes (Figure 3) with the occurrence of anomalous dynamical behavior. To this end, we use the *S* transform (ST) [*Stockwell et al*., 1996], which identifies in time the variability of a Fourier spectrum. The advantage of ST compared to other types of wavelet analysis is its unique relationship with the Fourier spectrum; that is, when integrated in time it reproduces the Fourier spectrum. We have used this property of the ST to evaluate the statistical significance of the variability in the time-frequency domain, following the approach already devised by *Sassi et al.* [2012]. Details of this methodology are described briefly in Appendix A.

We focus our analysis in the Jicamarca longitude sector in the latitudes north (0°N) and south (30°S) of the magnetic equator, which is located at 11°S. Figure 7 shows the ST amplitude spectrum of the zonal wind at 30°S and at the geographic equator, averaged in longitude between 275°E and 295°E, for the eastward propagating wave number 2 (Figures 7a and 7b) and wave number 3 (Figures 7c and 7d) at 120 km altitude. The dashed magenta line indicates 27 January 2009, the day in which anomalous behavior in TEC is detected. Whiteout frequency-time loci mask the values that are deemed not statistically significant (see Appendix A). The diurnal variations, DE2 and DE3, decrease in amplitude around the time of the SSW, especially at the equator (Figures 7b and 7d). SE2 and SE3 are not particularly strong at the equator, but they emerge as prominent tidal waves at 30°S (Figures 7a and 7c). In the case of wave number 2 (Figure 7a), SE2 is larger ahead of the SSW, with rapidly decreasing amplitude toward the SSW; after the SSW, on 27 January 2009 the amplitude of SE2 begins to increase slowly. The SE3 (Figure 7c) shows instead a behavior with modest amplitude approaching the SSW and a short-lived burst on 27 January 2009.

It is possible that the decrease in amplitude of the DE2 and DE3 tides along with amplification in the semidiurnal tides is responsible for the semidiurnal behavior in the TEC and vertical $E \times B$ drift velocity at the Jicamarca longitude, as shown in Figure 3. Because Jicamarca is located in the longitude sector in which the magnetic equator takes its largest excursion southward, it is quite likely that the SE2, with large amplitude and large vertical wavelength at 30°S, contributes to the variability of the equatorial ionospheric electric fields. The reason for the prominent amplification of the semidiurnal amplitude at the time of the SSW is not clear. *Sassi and Liu* [2014] have shown that traveling planetary wave behavior at times concurrent and following the SSW of January 2009 propagates toward the equator, providing a potential route to couple the high latitudes of boreal winter with the tropical tides. The actual physical mechanism responsible for this coupling remains unclear, and it may be due to the development of anomalous meridional gradients of the zonal flow at the times around an SSW [*McLandress*, 2002; *Sakazaki et al*., 2013].

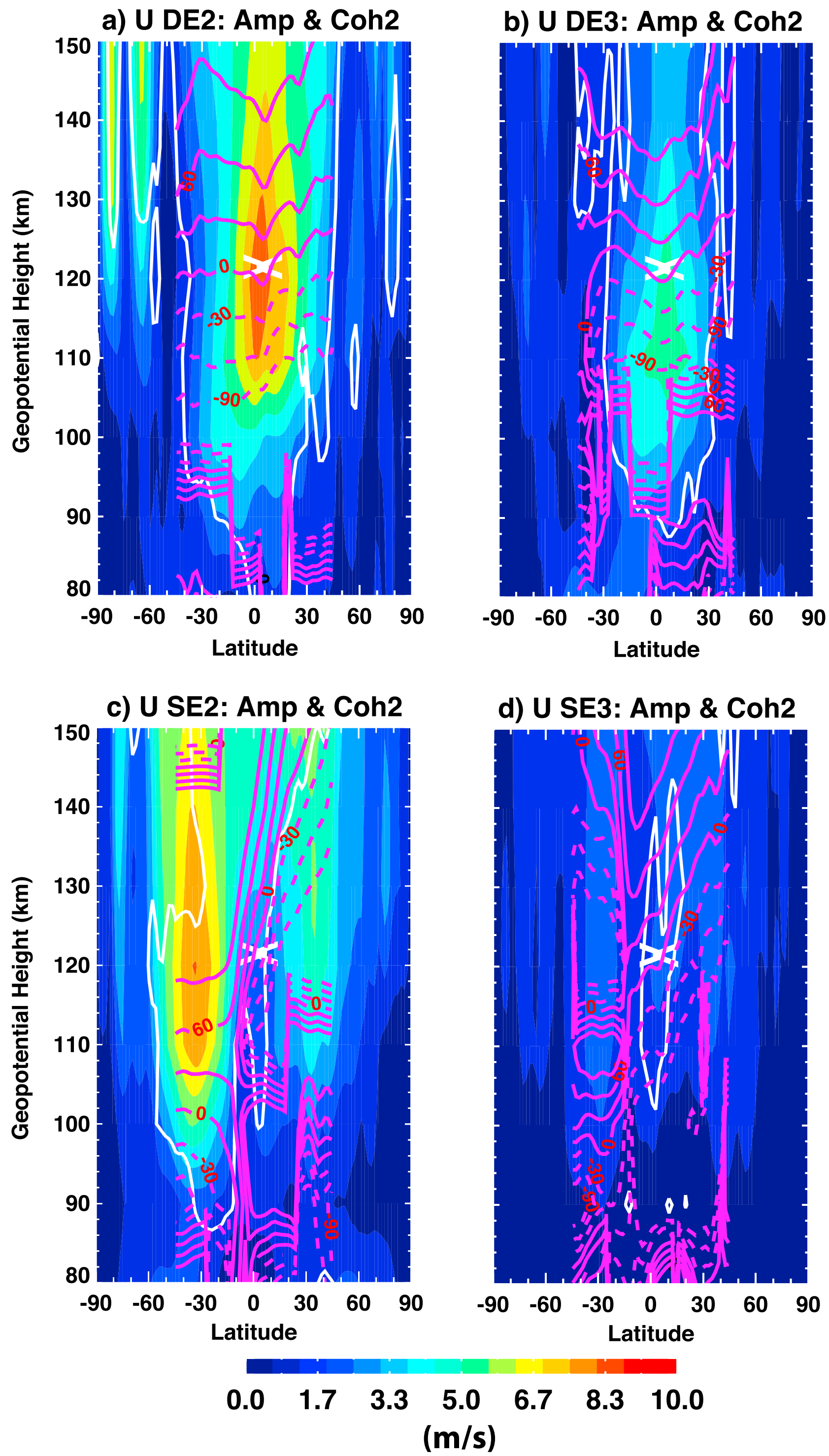

Figure 6. Height versus latitude amplitude in ms^{-1} and phase (red lines) obtained from the coherence analysis of the zonal wind, spectrally filtered for (a) DE2, (b) DE3, (c) SE2, and (d) SE3 tides. The white contours identify the regions where the spectral behavior is coherent with the base point (marked by an *X* in each panel) with a confidence greater than 99%. Contour interval in the phase is 30°.

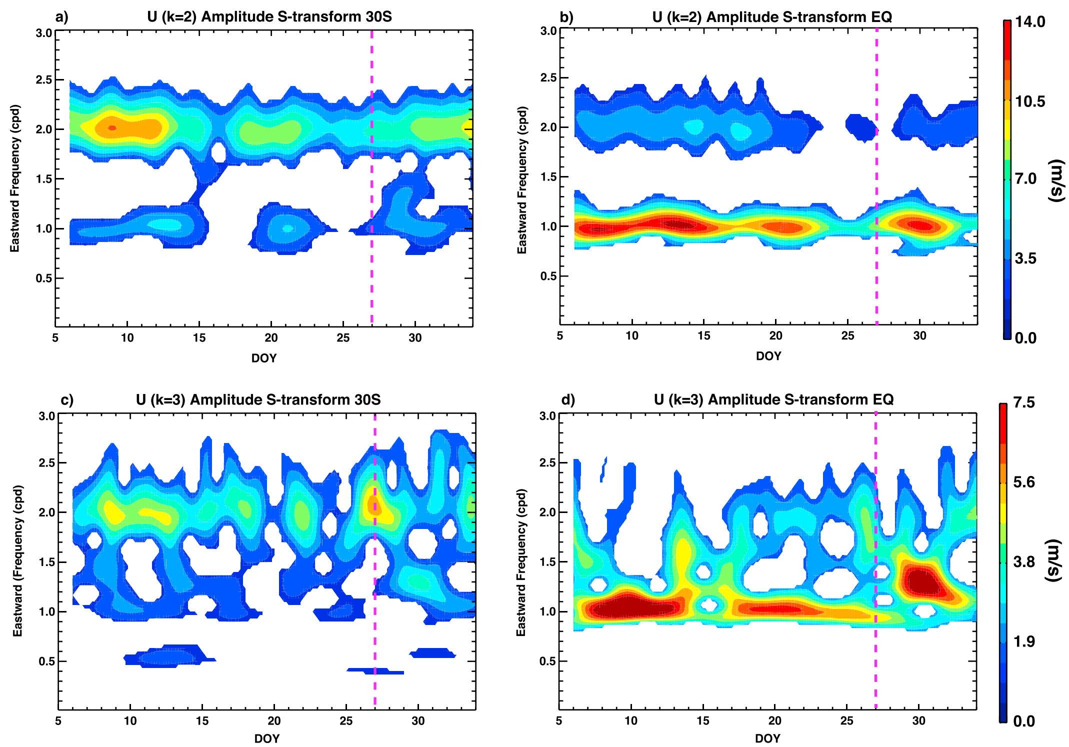

Figure 7. ST amplitude in ms^{-1} of the (a and c) zonal wind at 30°S and the (b and d) geographic equator in the longitude range between 275°E and 295°E at 120 km altitude for (Figures 7a and 7b) wave number 2 and (Figures 7c and 7d) wave number 3. The magenta vertical dashed line identifies the time of the largest effects in the plasma (27 January 2009). Masked out values correspond to the spectral amplitudes that are not deemed statistically significant. See Appendix A.

4. Discussion

The SAMI3/SD-WACCM-X simulations show that significant longitudinal variation in TEC and $E \times B$ drifts is introduced by nonmigrating tides. The longitudinal pattern changes on a day-to-day basis and is largely driven by variations in the DE2 and DE3 tides at *E* region altitudes. *Fang et al.* [2013] reported similar day-to-day behavior in simulations of September equinox using the Global Ionosphere Plasmasphere (GIP) model driven by the Whole Atmosphere Model (WAM). When the SAMI3 simulations are averaged over several days, a wave 3 pattern emerges when viewed at constant local time. These results are consistent with previous studies using space-based observations that indicate that the wave 3 is dominant during December solstice months [e.g., *Scherliess et al.*, 2008; *Fejer et al.*, 2008; *Kil et al.*, 2008]. Although the peak in the wave 3 pattern near 0°E longitude is consistent with the observations, the separation of the peaks, roughly ~90° longitude, is more consistent with a wave 4 pattern than the ~120° separation shown for example in the JPL TEC (Figure 1a). The reason for the discrepancy is due to the fact that the DE3 and DE2 tides in the zonal winds have nearly equal impact on the ionosphere during the 10 day period (6–15 January 2009); the nearly equal importance of the DE3 and DE2 tides leads to a superposition effect. *Kil et al.* [2011] illustrate this effect in their analysis of ROCSAT-1 vertical $E \times B$ drifts during July months (see their Figure 4), which matches the locations of our wave 3 crests quite well.

Despite the rather large amplitude of DE3 during the early part of January 2009, the average amplitude over the month is ~8 m s^{-1} at 110 km (Figure 5b) and is generally weaker than the DE2 (~12 m s^{-1}). Our results are in agreement with observational studies that indicate that DE3 is typically weaker than DE2 in the northern winter months. For example, using temperatures from TIMED/SABER and F_2 peak altitudes (h_mF_2) from COSMIC, *Pancheva and Mukhtarov* [2010] found that the DE3 was weakest in January and the observed wave 3 structure is forced by DE2 from the lower atmosphere and a stationary planetary wave 3 that is likely generated in situ. The amplitude of the DE3 tide in the SD-WACCM-X zonal winds is in good agreement with observations [*Oberheide and Forbes*, 2008] and other modeling studies [*Liu et al.*, 2013]. The DE2 amplitude is also in agreement with other models [*Maute et al.*, 2014; *Liu et al.*, 2013].

The SAMI3 TEC in the EIA maxima is biased high (+18%) as compared with the JPL TEC (Figure 1); this is not unexpected, given that previous comparisons of SAMI3 global mean TEC are systematically higher by ~20% [*Lean et al.*, 2014] and are attributed to a thick topside. Weak daytime drifts contribute to the lack of well-separated EIA crests, as compared with the JPL TEC. Both SD-WACCM-X and HWM14 winds yield zonal mean daytime drifts on the order of 10 $\mathrm{ms^{-1}}$ or about half that of the Scherliess-Fejer peak daytime drifts. Modeling studies indicate that the neutral winds are an important contributor to the strength of the vertical $E \times B$ drifts. For example, *Millward et al.* [2001] found that the daytime vertical drift is highly dependent on the magnitude and phase of the semidiurnal tidal component of the winds. *Maute et al.* [2012] used TIME-GCM to show that the E and F region winds below 200 km are the primary contributors to the magnitude of the vertical plasma drift. To understand how the winds affect the daytime drifts, we modulated the amplitudes of the diurnal, semidiurnal, and terdiurnal tides within HWM14 and found that increasing the amplitude of the diurnal tide or the semidiurnal tide had the effect of increasing the daytime upward drifts, although the semidiurnal tide had the additional effect of amplifying the nighttime upward drifts as well (not shown). Based on these results, it is likely that the weak semidiurnal tide in SD-WACCM-X contributes to the weak daytime $E \times B$ drifts in our SAMI3/SD-WACCM-X simulations. Of course, Hall and Pedersen conductivities are also important and can also impact the vertical drifts. The fact that the SAMI3/HWM14 daytime drifts are also weak may suggest that the E region conductivities in SAMI3 are underestimated. We note that the SAMI3 drifts are comparable to vertical $E \times B$ drifts produced by TIME-GCM simulations under solar minimum ($F_{10.7} = 75$) conditions, in which the drifts vary between 6 and 15 $\mathrm{m\,s^{-1}}$ between 14:00 and 15:00 LT [*Maute et al.*, 2012].

Our simulations with the SD-WACCM-X winds show that nonmigrating tides play a role in upward drifts at night, and such upward drifts have been observed by the Ion Velocity Meter on board the Communication/Navigation Outage Forecasting System (C/NOFS) [*Stoneback et al.*, 2011]. In particular, the C/NOFS vertical drifts during northern winter 2008–2009 show upward drifts at night at most longitudes [cf. *Stoneback et al.*, 2011, Figure 5], with median amplitude of 20 $\mathrm{m\,s^{-1}}$, which agrees well with our results.

Next, we consider our results for day-to-day variability during January 2009. *Forbes et al.* [2000] used data from over 100 ionosondes during 1967–1989 to quantify F region ionospheric day-to-day variability and found that under geomagnetically quiet conditions, the 1 sigma variability of the peak height of the ionosphere (N_mF_2) is ~25–35% for periods on the order of a few hours to a few days. Typically, there is more variability in the EIA region and at night. Similar variability has been found in other studies [e.g., *Rishbeth and Mendillo*, 2001; *Araujo-Pradere et al.*, 2004]. The JPL TEC data at the Jicamarca longitude (Figure 4) show a peak daytime variability of 30%. Our model results with the SD-WACCM-X winds yield 16% variability in TEC around 15:00–16:00 LT due to the lower atmosphere meteorology. The variability in N_mF_2 (not shown) is 14%; only 3% of this variability is due to solar and geomagnetic conditions, as evidenced by the SAMI3 runs using HWM14 winds. Other recent modeling studies using winds constrained by the lower atmosphere give similar results. *Fang et al.* [2013] used WAM winds to drive GIP simulations during solar moderate conditions ($F_{10.7} = 120$) and found N_mF_2 in the low latitudes to vary by ~13% and electron content between 90 and 1000 km to vary by 9%. *Liu et al.* [2013] using TIME-GCM with SD-WACCM-X winds constrained by NASA/MERRA reanalysis for the time period of January–February 2006 found ~23% standard deviation of N_mF_2 at 16:00 LT. The TIME-GCM/WACCM-X simulations include modulation of the thermosphere, whereas our study and the WAM/GIP use climatological neutral densities and temperatures. It is likely that including thermospheric variability will increase the day-to-day variations in the SAMI3/SD-WACCM-X simulations, and such runs will be performed in the near future.

The measured day-to-day variation of vertical $E \times B$ drifts tends to be on the order of 10 $\mathrm{m\,s^{-1}}$ [*Patra et al.*, 2012; *Stoneback et al.*, 2011; *Scherliess and Fejer*, 1999]. With TIME-GCM/WACCM-X, *Liu et al.* [2013] obtained a standard deviation of 4 $\mathrm{m\,s^{-1}}$ for daytime drifts. Our SAMI3/SD-WACCM-X daytime drifts vary on the order of 6 $\mathrm{m\,s^{-1}}$. With nonmigrating tides removed, the variability decreases to 4 $\mathrm{m\,s^{-1}}$. As demonstrated with the HWM14 simulations, the solar and geomagnetic contributions are less than 1 $\mathrm{m\,s^{-1}}$. It is possible that neither TIME-GCM nor SD-WACCM-X exhibits sufficient variability in the migrating tides at E region altitudes. But it is more likely that to capture the true variability at a stationary location, the resolution of the simulations would need to be increased.

The SAMI3/SD-WACCM-X simulations show a weak response to the SSW on 24 January 2009. The most likely reason for this result is that the SW2 tide is suspected to be a primary driver of the SSW effects in the

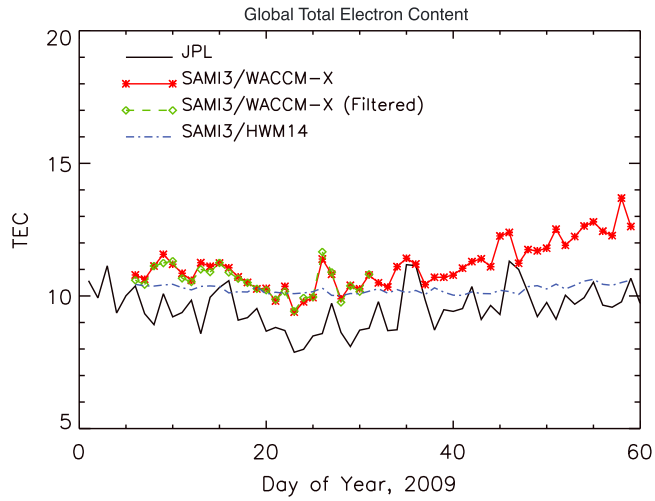

Figure 8. Daily global mean TEC over January–February 2009. The black line represents the JPL TEC. The red line with stars shows the results for SAMI3 with WACCM-X winds. The green line with diamonds shows the SAMI3 with filtered WACCM-X winds (only run for January 2009), and the blue dot-dashed line shows the TEC for the SAMI3 using climatological HWM14 winds.

ionosphere, based on previous modeling studies [e.g., *Fuller-Rowell et al.*, 2011; *Jin et al.*, 2008; *Pedatella et al.*, 2014b], but the SW2 tide in SD-WACCM-X is known to be significantly weaker than in other models including GAIA and WAM [*Pedatella et al.*, 2014a]. Causes may include specific model parameterizations or the vertical resolution. Another contributing factor to our results is that SD-WACCM-X does not include a lunar tide, which may be important for the January 2009 SSW event [*Forbes and Zhang*, 2012; *Pedatella et al.*, 2014a].

Interestingly enough, in the Jicamarca longitude, we do see a response to the SSW that is related to the nonmigrating tides. With the nonmigrating tides filtered out, the feature is not present. Upon further analysis we identify the semidiurnal nonmigrating tides (SE2 and SE3) as a possible driver of this change on 27 January 2009. An assessment of the relative roles of these nonmigrating tides is beyond the scope of the present study; here we point out the prominent presence of these modes in relation to the SSW. Thus, we have identified that nonmigrating tides also may contribute to the ionospheric response to the SSW, especially at specific longitudes. *Fang et al.* [2012] studied longitudinal variability during the January 2009 SSW and found that nonmigrating tides and planetary waves possibly lead to modulation of the phase structures at different longitudes.

It is not unexpected that the different models yield differing results in the study of the January 2009 SSW, especially given the large discrepancies in the simulation of the neutral atmosphere as presented by *Pedatella et al.* [2014a]. If anything, the study of this event by various models has provided an excellent opportunity to compare the models and identify areas of improvement, and we can better appreciate the complexities in coupling the lower atmosphere to the thermosphere/ionosphere.

One of the goals of our efforts to couple SAMI3 with an atmosphere model is to better capture the true variability in the ionosphere, which will ultimately lead to improvements in ionospheric forecasting. In previous work, we have performed simulations using the NRLSSI to specify the solar irradiance but used empirical models to specify the neutral winds and thermospheric composition [*Lean et al.*, 2014; *McDonald et al.*, 2014]. Without meteorological weather, we were able to match variations such as the 27 day rotation of the Sun, the annual oscillation, and the semiannual oscillation. But now we can close in on even smaller-scale variations. For example, in Figure 8 we show the global average TEC over January–February 2009. The black line represents the JPL GIM TEC. Using SAMI3/HWM14, the day-to-day variation is quite flat during this geomagnetically quiet period (blue dot-dashed line). With the introduction of the WACCM-X winds, we are able to capture the day-to-day variability coming from the lower atmosphere. The global mean variations are captured in the migrating tides (red line), and the addition of the nonmigrating tides (green line) does not have a significant global effect; thus, in our model simulations nonmigrating tides act to redistribute the plasma, while migrating tides carry energy into the ionosphere, resulting in changes in the global TEC on a daily basis.

5. Conclusions

In this study we have performed SAMI3 simulations of the ionosphere for January–February 2009 using winds from SD-WACCM-X that have been constrained by meteorological reanalysis. Additional runs during the same time period are performed for SD-WACCM-X winds with the nonmigrating tidal components removed, and a climatological run was performed using HWM14. Using our model simulations, we have looked at the impact of lower atmospheric tides on the structure and variability of the ionosphere. We also characterized ionospheric variability due to the SSW event on 24 January 2009. Our conclusions are summarized as follows:

1. DE2 and DE3 nonmigrating tides play an important role in the longitudinal structure of the low-latitude ionosphere and are mainly coupled in through the electrodynamics in the *E* region ionosphere via modulation of the vertical $E \times B$ drift. When averaged over several days, a combination of wave 3/wave 4 pattern emerges; the JPL TEC over the same period (6–15 January 2009) indicates that a wave 3 pattern is dominant, suggesting that the DE3 in WACCM-X is too strong. SAMI3 simulations with the SD-WACCM-X-filtered winds (migrating tides only) compare well with the climatological (HWM14) runs. So while there is ample room for improvement, our results show that the SD-WACCM-X winds with data assimilation up to 92 km are reasonable.
2. We looked at the day-to-day variability of the ionosphere in January 2009 at the Jicamarca longitude and found that TEC varies by 16%. About half of this variation is due to nonmigrating tides, with the other half due to the migrating tides. Only 1% of the variation is due to solar and geomagnetic effects during this quiet period at extreme solar minimum. The model captures about half of the variability observed in the JPL TEC, which is 30%, and is partly due to the use of climatological quantities for neutral density and temperature. The modeled $E \times B$ drift exhibits day-to-day variation of 5 m s^{-1}, in agreement with other models driven with lower atmospheric meteorology. Again, this is half of the observed variation of 10 m s^{-1}.
3. The SSW event had a minor impact on the modeled ionosphere and is possibly due to the weak amplitude of the SW2 tide in SD-WACCM-X, which has been identified as a main driver in other coupled model simulations. However, we do detect a semidiurnal feature in the $E \times B$ drifts at the Jicamarca longitude on 27 January 2009 with characteristics that match observations; the upward vertical drift is enhanced during the morning hours and turns negative in the afternoon. This feature is plausibly associated with the SE2 and SE3 nonmigrating tides. Contributions from these tides lead to longitudinal variations in the SSW impact on the ionosphere.

Appendix A

Sassi et al. [2012] have developed a method to evaluate the statistical significance of a geophysical spectrum in time. This method is based on the formulations and theories of *Fisher* [1929] and *Wilks* [2006]; it relies on the assumption that the background temporal variability (the null hypothesis) is described by an autoregressive process of the first order, whose frequency spectrum $\Sigma(\omega)$ is

$$\Sigma(\omega) = \frac{1\sigma_\varepsilon^2/N}{1+\rho^2-2\rho\cos(\omega)}, \tag{A1}$$

where $\sigma_\varepsilon{}^2$ is an equally distributed variance at all frequency and equivalent to a white spectrum, N is the number of samples in the time series, ρ is the lag-1 autocorrelation, and ω is the frequency in rad s^{-1}. At each frequency ω_i, the spectrum Ψ_i of a geophysical quantity $h(t)$ is deemed statistically significant at a level $(1-\alpha)$ if

$$\Psi_i^2 > \frac{\Sigma(\omega_i)\chi^2(1-\alpha)}{v}, \tag{A2}$$

where $\chi^2(1-\alpha)$ is the value of the chi-square distribution corresponding to a statistical significance level $(1-\alpha)$ with υ degrees of freedom. As discussed by *Fisher* [1929], the value α needs to be more stringent due to the lack of a priori knowledge of where the spectral peaks might occur. In practice, the effective value α^* that is used to evaluate $\chi^2(1-\alpha^*)$ is scaled by the number of independent frequencies in the spectrum (K^*); that is,

$$\alpha^* = \frac{\alpha}{K^*}. \tag{A3}$$

Stockwell et al. [1996] define the *S* transform (ST) as a phase correction to the continuous wavelet transform, and thus, the ST of a function $h(t)$ is defined as

$$S(\tau,f) = \int_{-\infty}^{+\infty} h(t)\frac{|f|}{\sqrt{2\pi}} e^{-\frac{(\tau-t)^2 f^2}{2}} e^{-i2\pi f t}\; dt, \tag{A4}$$

where f is the frequency in s^{-1}. An important property of the ST is that when integrated over the time domain τ it reproduces the Fourier spectrum of the function $h(t)$; that is,

$$\Psi(f) = \int_{-\infty}^{+\infty} S(\tau,f)\; d\tau. \tag{A5}$$

Using the property (A5) of the ST along with the method leading to (A2) to evaluate the statistical significance, we have calculated the spectral component of the ST from the time series of the model output and plotted only those that are deemed statistically significant with a confidence level of 99% with 20 degrees of freedom.

Acknowledgments
SAMI3 and SD-WACCM-X simulation output is archived at the Naval Research Laboratory. Global ionospheric maps of TEC are maintained by JPL. The Scherliess-Fejer model is available upon request from Ludgar Scherliess at Utah State University. Model output and TEC data sets are available from the authors upon request. S.M. and F.S. are supported by the Chief of Naval Research through NRL base funding. F.S. was partially supported by NASA/LWS grant NNH12AT21I. This work was also supported in part by a grant of computer time from the DOD High Performance Computing Modernization Program at the U.S. Navy DOD Supercomputing Resource Center (NAVO). Portions of this research were carried out at the Jet Propulsion Laboratory, California Institute of Technology, under a contract with the National Aeronautics and Space Administration. Sponsorship of the Heliophysics Division of NASA's Science Mission Directorate is gratefully acknowledged. Finally, we would like to thank Joseph Huba for providing us with the SAMI3 source code.

References

Akmaev, R. A., T. J. Fuller-Rowell, F. Wu, J. M. Forbes, X. Zhang, A. F. Anghel, M. D. Iredell, S. Moorthi, and H.-M. Juang (2008), Tidal variability in the lower thermosphere: Comparison of Whole Atmosphere Model (WAM) simulations with observations from TIMED, *Geophys. Res. Lett.*, *35*, L03810, doi:10.1029/2007GL032584.

Appleton, E. V. (1946), Two anomalies in the ionosphere, *Nature*, *157*, 691.

Araujo-Pradere, E. A., T. J. Fuller-Rowell, and D. Bilitza (2004), Ionospheric variability for quiet and perturbed conditions, *Adv. Space Res.*, *34*, 1914–1921.

Chau, J. L., B. G. Fejer, and L. P. Goncharenko (2009), Quiet variability of equatorial $E \times B$ drifts during a sudden stratospheric warming event, *Geophys. Res. Lett.*, *36*, L05101, doi:10.1029/2008GL036785.

Drob, D. P., et al. (2008), An empirical model of the Earth's horizontal wind fields: HWM07, *J. Geophys. Res.*, *113*, A12304, doi:10.1029/2008JA013668.

Drob, D. P., et al. (2015), An update to the horizontal wind model (HWM): The quiet time thermosphere, *Earth Space Sci.*, doi:10.1002/2014EA000089, in press.

Emmert, J. T., J. M. Picone, and R. R. Meier (2008), Thermospheric global average density trends, 1967–2007, derived from orbits of 5000 near-Earth objects, *Geophys. Res. Lett.*, *35*, L05101, doi:10.1029/2007GL032809.

England, S. L. (2011), A review of the effects of nonmigrating atmospheric tides on the Earth's low-latitude ionosphere, *Space Sci. Rev.*, doi:10.1007/s11214-011-9842-4.

England, S. L., T. J. Immel, E. Sagawa, S. B. Henderson, M. E. Hagan, S. B. Mende, H. U. Frey, C. M. Swenson, and L. J. Paxton (2006), Effect of atmospheric tides on the morphology of the quiet time, postsunset equatorial ionospheric anomaly, *J. Geophys. Res.*, *111*, A10S19, doi:10.1029/2006JA011795.

England, S. L., T. J. Immel, and J. D. Huba (2008), Modeling the longitudinal variation in the post-sunset far-ultraviolet OI airglow using the SAMI2 model, *J. Geophys. Res.*, *113*, A01309, doi:10.1029/2007JA012536.

Fang, T.-W., T. Fuller-Rowell, R. Akmaev, F. Wu, H. Wang, and D. Anderson (2012), Longitudinal variation of ionospheric vertical drifts during the 2009 sudden stratospheric warming, *J. Geophys. Res.*, *117*, A03324, doi:10.1029/2011JA017348.

Fang, T.-W., R. Akmaev, T. Fuller-Rowell, F. Wu, N. Maruyama, and G. Millward (2013), Longitudinal and day-to-day variability in the ionosphere from lower atmosphere tidal forcing, *Geophys. Res. Lett.*, *40*, 2523–2528, doi:10.1002/grl.50550.

Fejer, B. G., J. W. Jensen, and S.-Y. Su (2008), Quiet time equatorial *F* region vertical plasma drift model derived from ROCSAT-1 observations, *J. Geophys. Res.*, *113*, A05304, doi:10.1029/2007JA012801.

Fisher, R. A. (1929), Tests of significance in harmonic analysis, *Proc. R. Soc. London, Ser. A*, *125*, 54–59.

Forbes, J. M., and X. Zhang (1997), Quasi 2-day oscillations of the ionosphere: A statistical study, *J. Atmos. Sol. Terr. Phys.*, *59*(9), 1025–1034.

Forbes, J. M., and X. Zhang (2012), Lunar tide amplification during the January 2009 stratosphere warming event: Observations and theory, *J. Geophys. Res.*, *117*, A12312, doi:10.1029/2012JA017963.

Forbes, J. M., S. E. Palo, and X. Zhang (2000), Variability of the ionosphere, *J. Atmos. Sol. Terr. Phys.*, *62*, 685–693.

Forbes, J. M., X. Zhang, S. Palo, J. Russell, C. J. Mertens, and M. Mlynczak (2008), Tidal variability in the ionospheric dynamo region, *J. Geophys. Res.*, *113*, A02310, doi:10.1029/2007JA012737.

Fraser, G. J. (1977), The 5-day wave and ionospheric absorption, *J. Atmos. Terr. Phys.*, *39*, 121–124.

Fraser, G. J., and M. R. Thorpe (1976), Experimental investigations of ionospheric/stratospheric coupling in southern mid latitudes—1. Spectra and cross-spectra of stratospheric temperatures and the ionosphere f-min parameter, *J. Atmos. Terr. Phys.*, *38*, 1003–1011.

Fuller-Rowell, T., H. Wang, R. Akmaev, F. Wu, T.-W. Fang, M. Iredell, and A. Richmond (2011), Forecasting the dynamic and electrodynamic response to the January 2009 sudden stratospheric warming, *Geophys. Res. Lett.*, *38*, L13102, doi:10.1029/2011GL047732.

Fuller-Rowell, T. J., et al. (2008), Impact of terrestrial weather on the upper atmosphere, *Geophys. Res. Lett.*, *35*, L09808, doi:10.1029/2007GL032911.

Garcia, R. R., D. R. Marsh, D. E. Kinnison, B. A. Boville, and F. Sassi (2007), Simulation of secular trends in the middle atmosphere, 1950-2003, *J. Geophys. Res.*, *112*, D09301, doi:10.1029/2006JD007485.

Goncharenko, L. P., A. J. Coster, J. L. Chau, and C. E. Valladares (2010a), Impact of sudden stratospheric warmings on equatorial ionization anomaly, *J. Geophys. Res.*, *115*, A00G07, doi:10.1029/2010JA015400.

Goncharenko, L. P., J. L. Chau, H.-L. Liu, and A. J. Coster (2010b), Unexpected connections between the stratosphere and ionosphere, *Geophys. Res. Lett.*, *37*, L10101, doi:10.1029/2010GL043125.

Hagan, M. E., A. Maute, R. G. Roble, A. D. Richmond, T. J. Immel, and S. L. England (2007), Connections between deep tropical clouds and the Earth's ionosphere, *Geophys. Res. Lett.*, *34*, L20109, doi:10.1029/2007GL030142.

Hayashi, Y. (1971), A generalized method of resolving disturbances into progressive and retrogressive waves by space Fourier and time cross-spectral analyses, *J. Meteorol. Soc. Jpn.*, *49*, 125–128.

Hocke, K., and K. Schlegel (1996), A review of atmospheric gravity waves and traveling ionospheric disturbances: 1982–1995, *Ann. Geophys.*, *14*(9), 917–940.

Huba, J. D., G. Joyce, and J. A. Fedder (2000), SAMI2 (Sami2 is another model of the ionosphere): A new low-latitude ionosphere model, *J. Geophys. Res.*, *105*(A10), 23,035–23,053, doi:10.1029/2000JA000035.

Huba, J. D., G. Joyce, and J. Krall (2008), Three-dimensional equatorial spread *F* modeling, *Geophys. Res. Lett.*, *35*, L10102, doi:10.1029/2008GL033509.

Huba, J. D., G. Joyce, J. Krall, C. L. Siefring, and P. A. Bernhardt (2010), Self-consistent modeling of equatorial dawn density depletions with SAMI3, *Geophys. Res. Lett.*, *37*, L03104, doi:10.1029/2009GL041492.

Immel, T. J., E. Sagawa, S. L. England, S. B. Henderson, M. E. Hagan, S. B. Mende, H. U. Frey, C. M. Swenson, and L. J. Paxton (2006), Control of equatorial ionospheric morphology by atmospheric tides, *Geophys. Res. Lett.*, *33*, L15108, doi:10.1029/2006GL026161.

Jin, H., Y. Miyoshi, H. Fujiwara, and H. Shiagawa (2008), Electrodynamics of the formation of ionospheric wave number 4 longitudinal structure, *J. Geophys. Res.*, *113,* A09307, doi:10.1029/2008JA013301.

Jin, H., Y. Miyoshi, H. Fujiwara, H. Shinagawa, K. Terada, N. Terada, M. Ishii, Y. Otsuka, and A. Saito (2011), Vertical connection from the tropospheric activities to the ionospheric longitudinal structure simulated by a new Earth's whole atmosphere-ionosphere coupled model, *J. Geophys. Res.*, *116*, A01316, doi:10.1029/2010JA015925.

Jin, H., Y. Miyoshi, D. Pancheva, P. Mukhtarov, H. Fujiwara, and H. Shinagawa (2012), Response of migrating tides to the stratospheric sudden warming in 2009 and their effects on the ionosphere studied by a whole atmosphere-ionosphere model GAIA with COSMIC and TIMED/SABER observations, *J. Geophys. Res.*, *117*, A10323, doi:10.1029/2012JA017650.

Julian, P. R. (1972), Comments on the determination of significance levels of the coherence statistics, *J. Atmos. Sci.*, *32*, 836–837.

Kil, H., E. R. Talaat, S.-J. Oh, L. J. Paxton, S. L. England, and S.-J. Su (2008), Wave structures of the plasma density and vertical $E \times B$ drift in low-latitude *F* region, *J. Geophys. Res.*, *113*, A09312, doi:10.1029/2008JA013106.

Kil, H., Y.-S. Kwak, S.-J. Oh, E. R. Talaat, L. J. Paxton, and Y. Zhang (2011), The source of the longitudinal asymmetry in the ionospheric tidal structure, *J. Geophys. Res.*, *116*, A09328, doi:10.1029/2011JA016781.

Laštovička, J. (2006), Forcing of the ionosphere by waves from below, *J. Atmos. Sol. Terr. Phys.*, *68*, 479–497.

Lean, J. L., T. N. Woods, F. G. Eparvier, R. R. Meier, D. J. Strickland, J. T. Correira, and J. S. Evans (2011), Solar extreme ultraviolet irradiance: Present, past, and future, *J. Geophys. Res.*, *116*, A01102, doi:10.1029/2010JA015901.

Lean, J. L., S. E. McDonald, J. D. Huba, J. T. Emmert, D. P. Drob, and C. L. Siefring (2014), Geospace variability during the 2008–2009 Whole Heliosphere Intervals, *J. Geophys. Res. Space Physics*, *119*, 3755–3776, doi:10.1002/2013JA019485.

Liu, H.-L., et al. (2010), Thermospheric extension of the Whole Atmosphere Community Climate Model, *J. Geophys. Res.*, *115*, A12302, doi:10.1029/2010JA015586.

Liu, H.-L., V. A. Yudin, and R. G. Roble (2013), Day-to-day ionospheric variability due to lower atmosphere perturbations, *Geophys. Res. Lett.*, *40*, 665–670, doi:10.1002/grl.50125.

Mannucci, A. J., B. D. Wilson, D. N. Yuan, C. H. Ho, U. J. Lindqwister, and T. F. Runge (1998), A global mapping technique for GPS-derived ionospheric total electron content measurements, *Radio Sci.*, *33*(3), 565–582, doi:10.1029/97RS02707.

Mannucci, A. J., B. A. Iijima, U. J. Lindqwister, X. Q. Pi, L. J. Sparks, and B. D. Wilson (1999), GPS and ionosphere, in *Review of Radio Science 1996-1999*, edited by W. Ross-Stone, pp. 625–665, Wiley-IEEE Press, New York.

Marsh, D. R. (2011), Chemical-dynamical coupling in the mesosphere and lower thermosphere, in *Aeronomy of the Earth's Atmosphere and Ionosphere*, *IAGA Spec. Sopron Book Ser.*, vol. 2, pp. 3–17, Springer, Heidelberg, Germany, doi:10.1007/978-94-007-0326-1_1.

Maute, A., A. D. Richmond, and R. G. Roble (2012), Sources of low-latitude ionospheric E × B drifts and their variability, *J. Geophys. Res.*, *117*, A06312, doi:10.1029/2011JA017502.

Maute, A., M. E. Hagan, A. D. Richmond, and R. G. Roble (2014), TIME-GCM study of the ionospheric equatorial vertical drift changes during the 2006 stratospheric sudden warming, *J. Geophys. Res. Space Physics*, *119*, 1287–1305, doi:10.1002/2013JA019490.

McDonald, S. E., K. F. Dymond, and M. E. Summers (2008), Hemispheric asymmetries in the longitudinal structure of the low-latitude nighttime ionosphere, *J. Geophys. Res.*, *113*, A08308, doi:10.1029/2007JA012876.

McDonald, S. E., L. J. Lean, J. D. Huba, G. Joyce, J. T. Emmert, and D. P. Drob (2014), Long-term simulations of the ionosphere using SAMI3, in *Modeling the Ionosphere-Thermosphere System*, *Geophys. Monogr. Ser.*, vol. 201, edited by J. D. Huba, R. Schunk, and G. Khazanov, AGU, Washington, D. C., pp. 119–131.

McLandress, C. (2002), Seasonal variation of the propagating diurnal tide in the mesosphere and lower thermosphere. Part II: The role of tidal heating and zonal mean winds, *J. Atmos. Sci.*, *59*, 907–922.

Millward, G. H., I. C. F. Muller-Wodarg, A. D. Aylward, T. J. Fuller-Rowell, A. D. Richmond, and R. J. Moffett (2001), An investigation into the influence of tidal forcing on *F* region equatorial vertical ion drift using a global ionosphere-thermosphere model with coupled electrodynamics, *J. Geophys. Res.*, *106*(A11), 24,733–24,744, doi:10.1029/2000JA000342.

Miyoshi, Y., and H. Fujiwara (2003), Day-to-day variations of migrating diurnal tide simulated by a GCM from the ground surface to the exobase, *Geophys. Res. Lett.*, *30*(15), 1789, doi:10.1029/2003GL017695.

Namba, S., and K.-I. Maeda (1939), *Radio Wave Propagation*, 86 pp., Corona, Tokyo.

Oberheide, J., and J. M. Forbes (2008), Tidal propagation of deep tropical cloud signatures into the thermosphere from TIMED observations, *Geophys. Res. Lett.*, *35*, L04816, doi:10.1029/2007GL032397.

Pancheva, D., and P. Mukhtarov (2010), Strong evidence for the tidal control on the longitudinal structure of the ionospheric *F*-region, *Geophys. Res. Lett.*, *37,* L14105, doi:10.1029/2010GL044039.

Patra, A. K., P. P. Chaitanya, N. Mizutani, Y. Otsuka, T. Yokoyama, and M. Yamamoto (2012), A comparative study of equatorial daytime vertical $E \times B$ drift in the Indian and Indonesian sectors based on 150 km echoes, *J. Geophys. Res.*, *117*, A11312, doi:10.1029/2012JA018053.

Pedatella, N. M., et al. (2014a), The neutral dynamics during the 2009 sudden stratosphere warming simulated by different whole atmosphere models, *J. Geophys. Res. Space Physics*, *119*, 1306–1324, doi:10.1002/2013JA019421.

Pedatella, N. M., H.-L. Liu, F. Sassi, J. Lei, J. L. Chau, and X. Zhang (2014b), Ionosphere variability during the 2009 SSW: Influence of the lunar semidiurnal tide and mechanisms producing electron density variability, *J. Geophys. Res. Space Physics*, *119*, 3828–3843, doi:10.1002/2014JA019849.

Picone, J. M., A. E. Hedin, D. P. Drob, and A. C. Aikin (2003), NRLMSISE-00 empirical model of the atmosphere: Statistical comparisons and scientific issues, *J. Geophys. Res.*, *107*(A12), 1468, doi:10.1029/2002JA009430.

Richmond, A. D. (1995), Modeling equatorial ionospheric electric fields, *J. Atmos. Terr. Phys.*, *57*(10), 1103–1115.

Rishbeth, H., and M. Mendillo (2001), Patterns of F_2-layer variability, *J. Atmos. Sol. Terr. Phys.*, *63*, 1661–1680.

Sakazaki, T., M. Fujiwara, and X. Zhang (2013), Interpretation of the vertical structure and seasonal variation of the diurnal migrating tide from the troposphere to the lower mesosphere, *J. Atmos. Sol. Terr. Phys.*, *105*, 66–80.

Sassi, F., and H.-L. Liu (2014), Westward traveling planetary wave events in the lower thermosphere during solar minimum conditions simulated by SD-WACCM-X, *J. Atmos. Sol. Terr. Phys.*, *119*, 11–26, doi:10.1016/j.jastp.2014.06.009.

Sassi, F., R. R. Garcia, B. A. Boville, and H. Liu (2002), On temperature inversions and the mesospheric surf zone. *J. Geophys. Res.*, *107*(D19), 4380, doi:10.1029/2001JD001525.

Sassi, F., R. R. Garcia, and K. W. Hoppel (2012), Large-scale Rossby normal modes during some recent northern hemisphere winters, *J. Atmos. Sci.*, *69*, 820–839.

Sassi, F., H.-L. Liu, J. Ma, and R. R. Garcia (2013), The lower thermosphere during the northern hemisphere winter of 2009: A modeling study using high-altitude data assimilation products in WACCM-X, *J. Geophys. Res. Atmos.*, *118*, 8954–8968, doi:10.1002/jgrd.50632.

Scherliess, L., and B. G. Fejer (1999), Radar and satellite global equatorial *F* region vertical drift model, *J. Geophys. Res.*, *104*, 6829–6842, doi:10.1029/1999JA900025.

Scherliess, L., D. C. Thompson, and R. W. Schunk (2008), Longitudinal variability of low-latitude total electron content: Tidal influences, *J. Geophys. Res.*, *113*, A01311, doi:10.1029/2007JA012480.

Stockwell, R. G., L. Mansinha, and R. P. Lowe (1996), Localization of the complex spectrum: The *S* transform, *IEEE Trans. Signal Process.*, *44*, 998–1001.

Stoneback, R. A., R. A. Heelis, A. G. Burrell, W. R. Coley, B. G. Fejer, and E. Pacheco (2011), Observations of quiet time vertical ion drift in the equatorial ionosphere during the solar minimum period of 2009, *J. Geophys. Res.*, *116*, A12327, doi:10.1029/2011JA016712.

Wang, H., R. A. Akmaev, T.-W. Fang, T. J. Fuller-Rowell, F. Wu, N. Maruyama, and M. D. Iredell (2014), First forecast of a sudden stratospheric warming with a coupled whole-atmosphere/ionosphere model IDEA, *J. Geophys. Res. Space Physics*, *119*, 2079–2089, doi:10.1002/2013JA019481.

Wang, W., J. Lei, A. G. Burns, L. Qian, S. C. Solomon, M. Wiltberger, and J. Xu (2011), Ionospheric day-to-day variability around the Whole Heliosphere Interval in 2008, *Sol. Phys.*, *274*, 457–472, doi:10.1007/s11207-011-9747-0.

Wilks, D. S. (2006), *Statistical Methods in Atmospheric Sciences*, 627 pp., Academic Press, Oxford.

Woods, T. N., F. G. Eparvier, S. M. Bailey, P. C. Chamberlin, J. L. Lean, G. J. Rottman, S. C. Solomon, W. K. Tobiska, and D. L. Woodraska (2005), Solar EUV Experiment (SEE): Mission overview and first results, *J. Geophys. Res.*, *110*, A01312, doi:10.1029/2004JA010765.